what longer (2·403 and 2·473 Å). The difference between longer and shorter bonds is, however, not so striking as in our case. Fig. 2 is a packing diagram.

References

AVERBUCH-POUCHOT, M. T. (1978). *Acta Cryst.* B**34**, 3350–3351.

BAUR, W. H. (1970). *Trans. Am. Crystallogr. Assoc.* **6**, 129–155.

CROMER, D. T. & WABER, J. T. (1965). *Acta Cryst.* **18**, 104–109.

CRUICKSHANK, D. W. J. (1961). *J. Chem. Soc.* pp. 5486–5504.

DONNAY, G. & ALLMANN, R. (1968). *Acta Cryst.* B**24**, 845–855.

FERRARIS, G. (1970). *Rend. Soc. Ital. Mineral. Petrol.* **26**, 589–598.

GRAMACCIOLI, C. M., GRIFFIN, W. L. & MOTTANA, A. (1978). *Rend. Soc. Ital. Mineral. Petrol.* **34**. In the press.

KORNEV, A. N., BATALIEVA, N. G., MAKSIMOV, B. A., ILYUKHIN, V. V. & BELOV, N. V. (1972). *Sov. Phys. Dokl.* **17**, 88–90.

LAUGHON, R. B. (1971). *Am. Mineral.* **56**, 193–200.

LOUISNATHAN, S. J. & GIBBS, G. V. (1972*a*). *Am. Mineral.* **57**, 1614–1642.

LOUISNATHAN, S. J. & GIBBS, G. V. (1972*b*). *Am. Mineral.* **57**, 1643–1663.

MOORE, P. B. & BENNETT, J. M. (1968). *Science*, **159**, 524–526.

SHANNON, R. D. & PREWITT, C. T. (1969). *Acta Cryst.* B**25**, 925–946.

SMITH, J. V. & BAILEY, S. W. (1963). *Acta Cryst.* **16**, 801–811.

TOSSELL, J. A. & GIBBS, G. V. (1976). *Am. Mineral.* **61**, 287–294.

WAN, C., GHOSE, S. & GIBBS, G. V. (1977). *Am. Mineral.* **62**, 503–512.

Acta Cryst. (1979). B**35**, 2291–2300

The Nature of the Chemical Bonding in Boron Carbide, $B_{13}C_2$. II. Dynamic Deformation Densities and Valence Densities

BY A. KIRFEL, A. GUPTA AND G. WILL

Mineralogisches Institut der Universität Bonn, Lehrstuhl für Mineralogie und Kristallographie, Poppelsdorfer Schloss, 5300 *Bonn, Federal Republic of Germany*

(*Received* 9 *May* 1979; *accepted* 26 *June* 1979)

Abstract

The crystal structure of rhombohedral $B_{13}C_2$ is composed of two structural units, the linear C–B–C chain and the B_{12} icosahedron. Based on high-order (HO) refinement results, X–X maps of dynamic deformation densities and valence densities have been calculated for sections in both units. The influence of the scale factor and the local distribution of the variance of difference densities were investigated for the density distribution in the B–C bond of C–B–C, which lies in the hexagonal c axis and shows the largest deviations from the spherical free-atom model. Integrations of residual densities in the C–B–C unit yield experimental evidence for a theoretically postulated charge transfer of one electron towards the B_{12} icosahedron, providing a 10-electron closed-shell configuration for C–B–C. The charge distribution in and around the somewhat distorted B_{12} icosahedron is discussed in terms of a simple covalent-bond model.

0567-7408/79/102291-10$01.00

Introduction

In a previous paper (Kirfel, Gupta & Will, 1979; hereafter called part I) the crystal structure of $B_{13}C_2$ was studied by refinements of X-ray diffraction data. Both the conventional spherical free-atom model and the multipole expansion model (Hirshfeld, 1971; Harel & Hirshfeld, 1975) were used. This preceding paper contains the results from the various refinements and first conclusions concerning the bond character in $B_{13}C_2$. As a preliminary result no indication could be found that a charge transfer takes place from the C–B–C chain towards the B_{12} icosahedron. This had been demanded by Longuet-Higgins & Roberts (1955) in a theoretical paper on the bonding features in boron icosahedra. The extreme stability of the refractory borides, including boron carbide, is supposed to be based on such an electron transfer.

In a second part of the analysis we have now studied the dynamic deformation densities and valence den-

sities in sections of the structure. In the course of the evaluation of these difference densities, efforts were made to investigate the influence of the scale factor in more detail and to estimate the local accuracy of the deformation density distribution. Since the interaction in the C–B–C chain is the strongest in the structure it yields the largest observable bond effects, and therefore the C–B bond was taken as an example. Representative results of these calculations are given initially to convey an impression of the reliability of the subsequently presented difference density maps. Finally, integrations of the difference densities around the C–B–C chain were undertaken with the aim of tracing the charge character of this strongest structural unit.

Dynamic deformation densities

Since the structure of $B_{13}C_2$ is centrosymmetric, the dynamic deformation density distribution can be calculated by the Fourier summation:

$$\Delta\rho(\mathbf{r}) = \frac{2}{V}\sum_{\mathbf{h}} [F_o(\mathbf{h})/k - F_c^{\mathrm{HO}}(\mathbf{h})] \cos [2\pi\mathbf{h}.\mathbf{r}], \qquad (1)$$

where k is the scale factor obtained from the structure refinement. The summation is equivalent to an X–X synthesis

$$\Delta\rho(\mathbf{r}) = \frac{1}{k}\rho_o^u(\mathbf{r}) - \rho_c^{\mathrm{HO}}(\mathbf{r}) \qquad (2)$$

with ρ_o^u the unscaled observed electron density and ρ_c^{HO} the calculated density using HO refinement parameters. The F_c values were calculated with the positional and thermal parameters of the HO2 refinement ($\sin\theta/\lambda \geq 0{\cdot}75$ Å^{-1}) of paper I. The Fourier summation was limited to reflections with $s \leq 0{\cdot}80$ Å^{-1} since high-angle reflections hardly contain scattering contributions of charge accumulations due to bonding, and the addition of such reflections to difference density calculations merely increases statistical noise.

Valence densities

Valence densities represent the density distribution of the bonding electrons. They are obtained in a similar way as deformation densities by subtracting the spherical electron distributions of the atomic closed-shell cores from the observed density:

$$\Delta\rho_{\mathrm{val}}(\mathbf{r}) = \frac{1}{k}\rho_o^u(\mathbf{r}) - \rho_c^{\mathrm{core}}(\mathbf{r}). \qquad (3)$$

The summation corresponding to (1) must include the $F(000)$ contribution.

In the present case the $F_c^{\mathrm{core}}(\mathbf{r})$ values were calculated with the scattering factor curves of the closed 1s electron shells of B and C taken from *International Tables for X-ray Crystallography* (1974). Thus, the densities of the K shells were subtracted from the observed density leaving the thermally smeared distribution of the 2s and 2p electrons of the B and C atoms.

The scale factor

The calculation of the deformation density requires correct scaling of the observed density ρ_o^u, *i.e.* of $F_o(\mathbf{h})$. It is well known that errors in the scale factor introduce systematic errors in the deformation density maps proportional to the locally observed density. This affects greatly the regions around the atomic positions, while the regions well away from the atomic centers, where bond densities are to be expected, remain almost unaffected. In order to obtain a quantitative measure, we have studied in more detail the influence of the scale factor on the linear deformation density distribution along B(3)–C, where the strongest bond in the structure is found (see part I). The results are depicted in Fig. 1. All curves were calculated with the same HO2 parameters but with different scale factors. The general feature is a trough at the site of the nucleus of B(3), an approximately 1·25 e Å^{-3} higher density at C, and a large pile-up of bond density (~1 e Å^{-3}) between the atoms. This strong B–C interaction was already indicated by the short B–C bond distance of 1·438 Å (part I). The relative distribution of the difference density at the atomic positions corresponds to the higher electronegativity of C (2·55) compared to that of B (2·07).

The scale factors considered range from 0·479 (all-data refinement) to 0·450 (HO2 refinement), which corresponds to a decrease of 6%. This considerable difference demonstrates the strong model dependency of the scale factor, and the inadequacy of the spherical free-atom model for the fit to the observed density. The smaller scale factor (from the HO2 refinement)

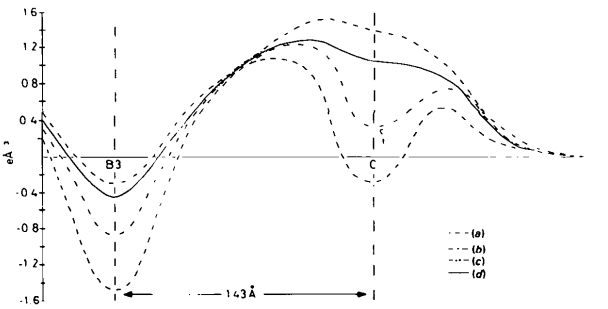

Fig. 1. Dynamic deformation density distribution along B(3)–C calculated with HO2 parameters and scale factors from (*a*) all-data refinement (0·479), (*b*) HO2 refinement (0·450), (*c*) HO2 refinement adjusted to LO data (0·461), and (*d*) multipole expansion refinement (0·453).

produces an increase of the deformation densities at the atomic sites of about 1·5 e Å^{-3}. Away from the atomic positions the deformation density is well established. The uncertainty resulting from the scaling increases on approaching the atomic centers and finally amounts to the above figure. Since the experimental determination of the scale factor is often impractical, as it is also in the present case, one has to decide which scale factor should be used for calculating deformation density maps with the highest degree of reliability.

Stevens & Coppens (1975) showed that conventional refinements, where all or low-order (LO) data are fitted to a spherical-atom model with HF scattering factors, in general yield scale factors which are too high in comparison with experimental values. In their paper the scale factors of four HO refinements were found to be up to 8% smaller than the scale factors from all or LO data refinements, and the HO scale factors agreed well within 1% with the averaged experimental scale factors measured by three independent methods. In a similar way scale factors obtained from the refinement of improved models, like scattering factors composed of cores and STO valence orbitals or variable scattering factor shapes, were close to the experimental values. The authors concluded that, in cases where no experimental scale factor is available, the scale factors obtained from HO refinements or from refinements with improved models are to be recommended for the evaluation of difference densities. The essential correctness of scale factors obtained from refinements with multipole expansion, representing an improved model, was also pointed out by Thomas (1978).

The scale-factor results of this study (part I) fit well into this picture. Both the HO2 scale factor (0·450) and the scale factor derived from the multipole expansion refinement (0·453) are the same, *i.e.* they agree within the limits of tolerance and are about 6% smaller than the all-data scale factor (0·479). For the difference density calculations we have therefore used the scale factor from the multipole expansion refinement. From the above discussions and in agreement with the experiences of Stevens & Coppens we estimate the accuracy of this value to be better than 2%.

The accuracy of the dynamic deformation density

The scale factor is an important parameter for the reliability of difference maps, but not the only one. We have therefore investigated the accuracy of the dynamic deformation density along B(3)–C in more detail. Estimates of the local standard deviation of $\Delta\rho$ were assessed by two methods (Stevens & Coppens, 1976; Rees, 1976, 1978). According to Stevens & Coppens the variance of the difference density is composed of three terms:

$$\mathrm{var}\,[\Delta\rho(\mathbf{r})] = \frac{1}{k^2}\,\mathrm{var}\,[\rho_o^u(\mathbf{r})] + \mathrm{var}\,[\rho_c(\mathbf{r})] + \frac{1}{k^2}\,\mathrm{var}\,(k)\,\frac{1}{k^2}\,[\rho_o^u(\mathbf{r})]^2. \quad (4)$$

The first term contains the variances of the observed structure factors (Cruickshank, 1949) and the second term the variance of ρ_c. For the calculation of the latter, Stevens & Coppens proposed to represent ρ_c in analytical form as a superposition of the individual thermally smeared atomic density distributions. Then ρ_c can be calculated by a Fourier transformation of the analytical scattering-factor functions (*International Tables for X-ray Crystallography*, 1974) multiplied by the isotropic temperature factor expressions. Considering correlations only between the refined atomic parameters and the scale factor, one obtains:

$$\mathrm{var}\,[\rho_c(\mathbf{r})] = \sum_m \left(\frac{\partial\rho_c}{\partial p_m}\right)^2 \mathrm{var}\,(p_m) + 2\sum_m \left(\frac{\partial\rho_c}{\partial p_m}\right)\sigma(p_m)\rho_o^u(\mathbf{r})\frac{\sigma(k)}{k}\,\gamma(p_m,k), \quad (5)$$

where $\gamma(p_m,k)$ are the correlation coefficients and $\sigma(p_m)$ the e.s.d.'s of the refined parameters p_m. The derivatives can be calculated from the analytical $\rho_c(\mathbf{r})$ expression.

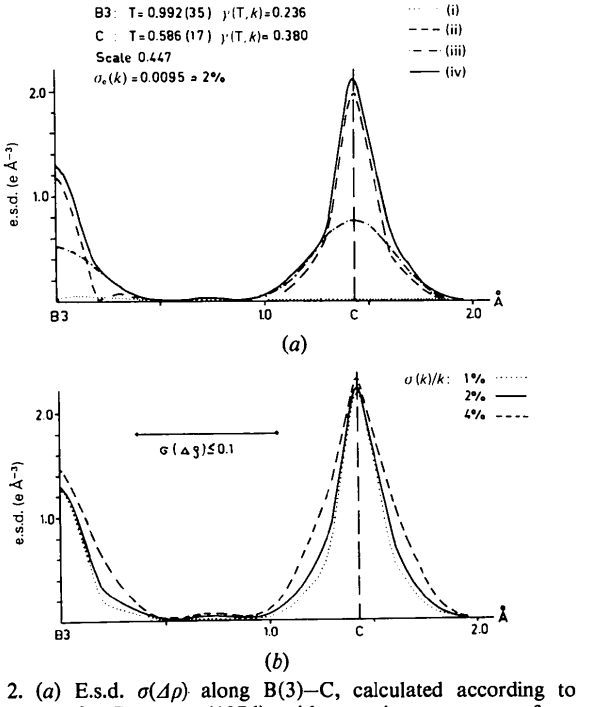

Fig. 2. (*a*) E.s.d. $\sigma(\Delta\rho)$ along B(3)–C, calculated according to Stevens & Coppens (1976) with atomic parameters from refinement with isotropic temperature factors. (i) $\sigma(\rho_o)$, (ii) $\sigma(k)/k$ contribution, (iii) $\sigma(\rho_c)$, (iv) total $\sigma(\Delta\rho)$. (*b*) variation of $\sigma(\Delta\rho)$ with $\sigma(k)/k$. All other parameters are as in (*a*).

The last term $\sigma(k)/k$ contains both the statistical error from the experiment and the error introduced by the inadequacy of the refinement model. Hence, $\sigma(k)$ can only be estimated and we have assumed a ratio of 2% for $\sigma(k)/k$. With this value the distribution of $\sigma(\Delta\rho)$ along B(3)—C was calculated according to (4) with the atomic parameters taken from a refinement with isotropic temperature factors. The result is depicted in Fig. 2(*a*). $\sigma[\rho_o(\mathbf{r})]$ is $< 0{\cdot}02$ e Å^{-3} throughout the cell. The dominating contributions to $\sigma(\Delta\rho)$, which shows large peaks at the atomic positions, stem from $\sigma(\rho_c)$ and $\sigma(k)/k$. The influence of a variation of $\sigma(k)/k$ on the total $\sigma(\Delta\rho)$ is depicted in Fig. 2(*b*). Increase or decrease of $\sigma(k)$ leads to only moderate alterations of the peak heights and to a slight expansion or contraction of the peak profiles, thus yielding smaller or larger areas of $\sigma(\Delta\rho)$ below a given level. Hence, the estimate of $\sigma(\Delta\rho)$ is clearly dominated by $\sigma(\rho_c)$ in this case, which is essentially based on the analytical scattering-factor curves of the atoms.

In the second method given by Rees (1978) the variance of $\Delta\rho$ is described by four terms:

$$\operatorname{var}[\Delta\rho(\mathbf{r})] = \operatorname{var}[\rho_o(\mathbf{r})] + \left\{\left[\frac{\rho_o^u(\mathbf{r})}{k}\right]^2 - 2\frac{\rho_o^u(\mathbf{r})}{k}\cdot\rho_c(\mathbf{r})\right\} \times \frac{\sigma_o^2(k)}{k} + \sum_i\sum_j A_i(\mathbf{r})\,A_j(\mathbf{r})\,\sigma(p_i)\,\sigma(p_j) \cdots \gamma(p_i,p_j) + \left[\frac{\rho_o^u(\mathbf{r})}{k}\right]^2\sigma_{\mathrm{mod}}^2(k)/k^2. \tag{6}$$

In this formulation the error introduced by the scale factor is split up into the statistical uncertainty $\sigma_o(k)$ (second term) and the model-dependent error $\sigma_{\mathrm{mod}}(k)$ (fourth term), which again can only be estimated. In contrast to the first method the variance of $\rho_c(\mathbf{r})$ is not deduced from an analytical expression of $\rho_c(\mathbf{r})$ but from the actual $\rho_c(\mathbf{r})$ as a result of a Fourier synthesis based on the F_c values. Taking all possible parameter correlations into account var$[\rho_c(\mathbf{r})]$ is given by the third term of (6). The $A_i(\mathbf{r})$ are:

$$A_i(\mathbf{r}) = \frac{\partial\rho_c(\mathbf{r})}{\partial p_i} + \frac{\rho_o^u(\mathbf{r})}{k}\frac{\partial k}{\partial p_i}, \tag{7}$$

with $\partial\rho_c/\partial p_i$ resulting from a Fourier synthesis performed with the derivatives $\partial F_c(\mathbf{h})/\partial p_i$ and

$$\frac{1}{k}\frac{\partial k}{\partial p_i} = \sum_{\mathbf{h}}\left[w(F_o^u/k - 2F_c)\frac{\partial F_c}{\partial p_i}\right]\Big/\sum_{\mathbf{h}} wF_c^2. \tag{8}$$

With

$$w = \frac{k^2}{\sigma^2(F_o^u)} \quad\text{and}\quad \frac{\sigma_o^2(k)}{k^2} = \left(\sum_{\mathbf{h}} wF_c^2\right)^{-1},$$

the second term of (7) transforms to:

$$\frac{\rho_o^u(\mathbf{r})}{k}\frac{\partial k}{\partial p_i} = \rho_o^u(\mathbf{r})\,\sigma_o^2(k)\sum_{\mathbf{h}}\frac{1}{\sigma^2(F_o^u)} \times\left[\frac{F_o^u}{k} - 2F_c\right]\frac{\partial F_c}{\partial p_i}. \tag{9}$$

The derivatives $\partial F_c/\partial p_i$ can be extracted from any conventional least-squares program like *ORFLS* (Busing, Martin & Levy, 1962); however, the calculation of numerous Fourier syntheses with $\partial F_c/\partial p_i$ coefficients is rather time-consuming. For comparison, $\sigma[\Delta\rho(\mathbf{r})]$ along B(3)—C was calculated with the same isotropic refinement results as in the first method. The four curves in Fig. 3 represent $\sigma(\Delta\rho)$ calculated with $\sigma_{\mathrm{mod}}(k)/k$ values of 0, 1, 2, and 4% respectively. Thus the first curve shows the contributions of the first three terms of (6) solely, and the other three curves demonstrate the influence of an increasing $\sigma_{\mathrm{mod}}(k)/k$ ratio. An analysis of the individual contributions to the first curve reveals that the third term of (6) is the dominant one and is governed itself by the contribution of the isotropic temperature factor of the C atom. This result corresponds to the strong anisotropic electron distribution of carbon due to its bonding and thermal vibrations.

A comparison of the two $\sigma(\Delta\rho)$ estimates shows that the method proposed by Stevens & Coppens yields too high values at the atomic positions for the case investigated. This must be a consequence of using the analytical scattering-factor curves of neutral B and C for the calculation of var$[\rho_c(\mathbf{r})]$, which cannot deal properly with the cusp densities of the bonded atoms. For the bond regions both estimates yield the same result, namely that $\sigma(\Delta\rho)$ is $< 0{\cdot}1$ e Å^{-3} outside spheres of approximately 0·35 Å radius around the atomic positions. This radius corresponds to the resolution limit of this study (Wilson, 1979).

At the midpoint between the atoms $\sigma(\Delta\rho)$ never exceeds 0·05 e Å^{-3}. This figure may serve to attach significance to the features in the deformation density

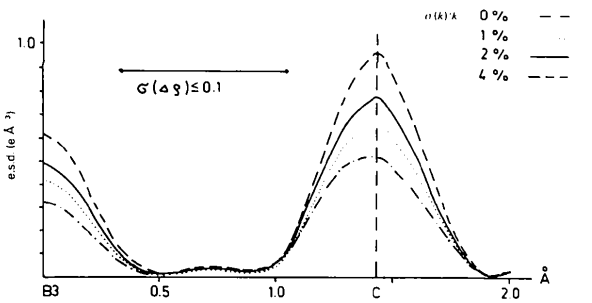

Fig. 3. E.s.d. $\sigma(\Delta\rho)$ along B(3)—C, calculated according to Rees (1978), with atomic parameters from refinement with isotropic temperature factors.

maps in any region. Since both estimates are based on the isotropic model, one can assume $\sigma(\Delta\rho)$ is still overestimated. The true uncertainty will be even smaller and the regions of significance will be larger than indicated in Fig. 3.

Results of the dynamic deformation densities and valence densities

The deformation density maps show positive densities of about 0·6 e Å^{-3} at all B atom positions of the icosahedron. This is comparable to $\sigma(\Delta\rho)$ at B(3) (Fig. 3). Generally, one can avoid such peaks by adjusting the scale factor, and an estimate of the proper scale factor to avoid deformation density at the icosahedral B atom positions yielded $k = 0{\cdot}466$. This corresponds to a 3% increase of the best value (0·453) derived from refinements (part I). According to the scale-factor discussion (part I) this value seems too high and the increment is beyond the e.s.d. of k as discussed before. Therefore we kept the chosen scale factor of $k = 0{\cdot}453$ for the calculations of the ensuing density maps.

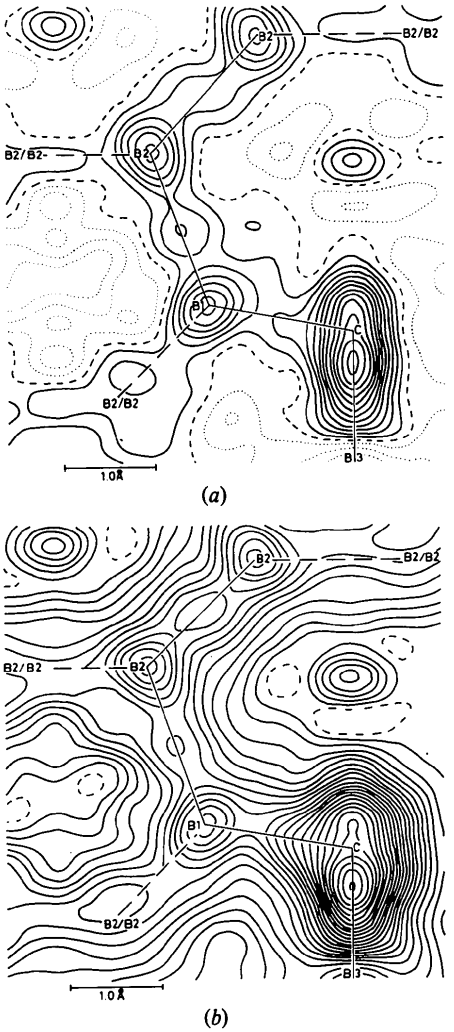

Fig. 4. (*a*) Dynamic deformation density distribution in the B(3), C, B(1), B(2) plane. Levels are at 0·05 e Å^{-3}, negative contours are dotted. (*b*) Valence density distribution. Levels are at 0·1 e Å^{-3}, negative contours are dotted.

(*a*) *The* C–B–C *chain*

Fig. 4(*a*) and (*b*) shows the dynamic deformation density and the valence density respectively in the mirror plane containing the atoms of one asymmetric unit of the structure.

Two C atoms and B(3) are on the *c* axis with B(3) at the inversion center at $0,0,\frac{1}{2}$. These sections contain, therefore, the unique half of the C–B–C chain, one structural unit, and part of the B_{12} icosahedron, the other unit. The deformation density viewed perpendicular to *c* clearly shows a significant charge transfer *within* the C–B–C chain from B towards C (compare also Fig. 1) with a flat maximum deformation density of 1·2 e Å^{-3} at 1 Å from B(3). This accumulation can be associated with the overlap of an *sp* orbital of B(3) with an sp^3 orbital of C. The valence density (Fig. 4*b*) is of similar appearance. It shows that the deformation density describes the general features of the valence-electron distribution quite well.

Starting from B(3) the valence density steadily increases on approaching C, and therefore it is impossible to decide on a reasonable partitioning of the atoms in terms of the density distributions between B(3) and C. On the other hand, there are distinct saddle points of the density distribution between the C–B–C chain and the icosahedron, *i.e.* between C and B(1),

Table 1. *Number of electrons Z associated with* C–B(3)–C, B(3), *and* C

For volumes of integration and molecular partitioning, see text.

	Method	C–B(3)–C	B(3)		C	
	LO refinement (part I)	17·14	4·58		6·28	
	Multipole expansion (part I)	17·08	1·43		7·83	
	$\int_A \rho_c(\mathbf{r})\,dv$	16·89	(*a*)	(*b*)	(*a*)	(*b*)
(I)	$\int_A \Delta\rho(\mathbf{r})\,dv$	17·20	4·41	4·36	6·40	6·42
(II)	$\int_A \rho_o(\mathbf{r})\,dv$	15·86	4·08	4·59	5·89	5·63
(III)	$\int_C \rho_o(\mathbf{r})\,dv$	17·07	3·74	4·68	6·66	6·19
(IV)	$\int_A \rho_{val}(\mathbf{r})\,dv$	15·79	3·89	4·80	5·95	5·49
(V)	$\int_B \rho_{val}(\mathbf{r})\,dv$	15·65	3·87	4·79	5·89	5·43
(VI)	$\int_C \rho_{val}(\mathbf{r})\,dv$	16·04	3·44	4·18	6·30	5·93
	Mean (II–VI)	16·08	3·80	4·61	6·14	5·73

which serve for the separation of the two structural building blocks. The problems of molecular partitioning have been discussed by Smith (1977).

For evaluating the charge character of both the C–B–C chain and the individual C and B(3) atoms we performed three different integrations of the density distributions over different volumes. The results in the form of atomic numbers of electrons are listed in Table 1 with the figures obtained from the LO refinement with variable multiplicities (part I).

(i) Volume *A*: for the definition of the volume of integration we followed the procedure outlined by Bader (1975). The volume is composed of disk layers containing hexagonal volume elements 0·1 × 0·1 × 0·1 Å with the disk radii defined by the line following the steepest descent from the saddle point between C and B(1) in the dynamic deformation density (Fig. 4*a*). The resulting volume has rotational symmetry and a mirror plane perpendicular to the rotation axis. Its significance was checked by integrating $\rho_c(\mathbf{r})$, yielding a charge of 16·89 e compared to the theoretical value of 17 e ($\Delta Z \triangleq 0{\cdot}65\%$).

(ii) Volume *B*: the same as *A*, but with disk radii taken from the valence density (Fig. 4*b*).

(iii) Volume *C*: in this approach the volume simply consists of a cylinder of 1·0 Å radius and two half spheres of the same radius at the top and bottom. The radius corresponds to the distance of the saddle point on the C–B(1) bond (Fig. 4*a*) from the *c* axis.

Molecular partitioning: (*a*) Taking the charge values of the individual disks from the integration $\int_A \rho_c(\mathbf{r})\mathrm{d}V$ it was found that the 11 inner layers around B(3) contained 4·98 e. Hence one possible molecular partitioning scheme can be achieved by confining the density integration for B(3) to these inner layers. This is identical to assigning a radius $r_B = 0{\cdot}55$ Å in the B(3)–C direction. (*b*) A method proposed by Kurki-Suonio & Salmo (1971) is based on the analysis of the radial charge density $4\pi r^2\rho_o(\mathbf{r})$ *vs* *r*. The minimum, which occurs prior to the rise due to the neighboring atom, may serve to define the atomic radius. The radii derived from this method were $r_B = 0{\cdot}75$ and $r_C = 0{\cdot}65$ Å, which add to 1·4 Å [B(3)–C = 1·43 Å]. Such a partitioning between B(3) and C corresponds to a density integration for B(3) comprising the 15 inner layers of the above-defined volumes.

The results of Table 1 corroborate, although in a qualitative way, the positive character of B(3). For the C atom the situation is less clear. According to the partitioning schemes one obtains either a negative charge (*a*) or a positive charge (*b*). For the total number of electrons in the C–B–C chain the integration of the deformation density did not give evidence for a charge deficit in agreement with the earlier refinement results (part I). On the other hand, integrations performed with ρ_o and ρ_{val} led to lower estimates of both B(3) and C charges and yielded total numbers of electrons which average to 16·08 e. The mean values of the individual atomic charges are $B(3)^{1\cdot2+}$ and $C^{0\cdot14-}$ (partitioning *a*), $B(3)^{0\cdot39+}$ and $C^{0\cdot27+}$ (partitioning *b*). This finding indicates that the chain is in a closed-shell configuration with 10 valence electrons, resulting from a charge transfer of 1 electron towards the B_{12} icosahedron. Consequently, a formal notation of boron carbide as $(CBC)^+B_{12}^-$ seems acceptable. Thus the evaluation of the charge character of the C–B–C chain gives experimental evidence for the Longuet-Higgins & Roberts (1955) hypothesis of charge transfer in order to stabilize the B_{12} icosahedron. For the bonding within the chain we can conclude that the charge difference of the B and C atoms provides additional electrostatic forces for the stabilization of the $(CBC)^+$ unit.

Following the *c* axis along the B(3)–C direction both density distributions (Fig. 4*a*,*b*) show a small charge accumulation with a maximum valence density of 0·6 e Å^{-3} approximately at the center of the large cavity ($z = 0{\cdot}7709$) between the icosahedra and the chain. A refinement with all reflections putting a small adjustable percentage of carbon into this position yielded a charge of 0·16 e $\triangleq$ 0·027 carbon atoms ($B_{iso} = 0{\cdot}79$ Å^2). If we assume that the excess charge on the *c* axis is due to contamination of the sample, *e.g.* statistically distributed carbon, the degree of such excess carbon content must be extremely small in agreement with the claimed stoichiometry of the compound. On the other hand, it is not impossible to consider the charge accumulation as the result of a long-range interaction between C and the three B(2) atoms of the above-lying icosahedron. This question deserves further attention and experiments with other crystals.

(*b*) *The* B_{12} *icosahedron*

The surface of the B_{12} icosahedron consists of 20 triangles, of which three are unique (Fig. 5). Figs. 6, 7

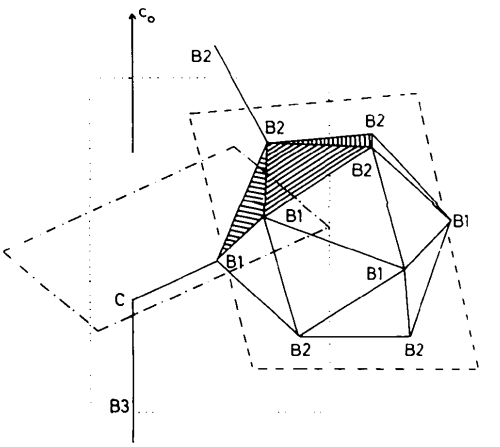

Fig. 5. The orientations of the difference density sections with respect to the structural units: dashed triangles Figs. 6, 7, 8; ··· Fig. 4(*a*,*b*); - - - Fig. 9; - · - Fig. 10.

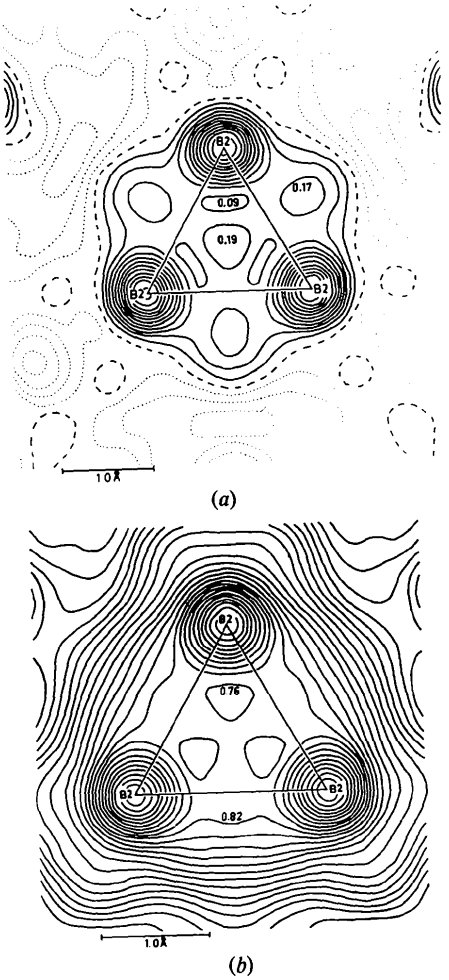

Fig. 6. (*a*) Dynamic deformation density distribution in the plane through B(2)–B(2)–B(2) (triangle I). Levels are at 0·05 e Å^{-3}, negative contours are dotted. (*b*) Valence density distribution; plot conditions are as in (*a*).

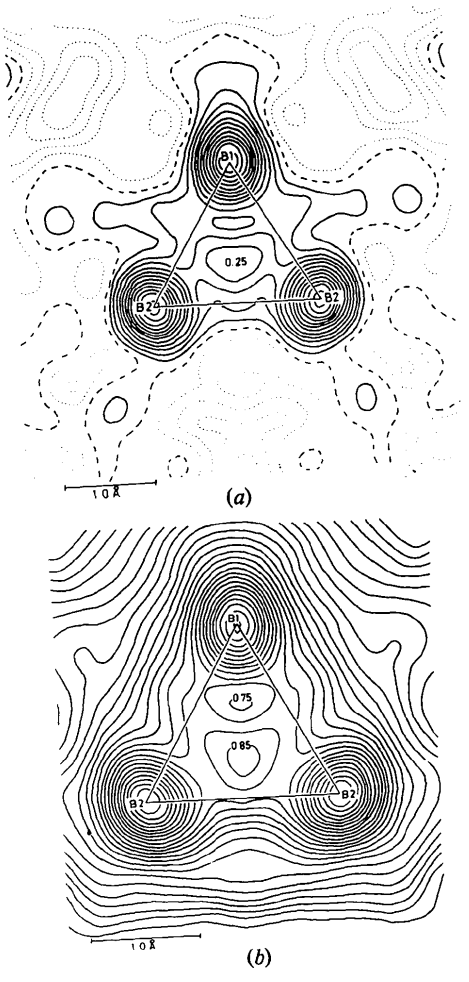

Fig. 7. (*a*) Dynamic deformation density distribution in the plane through B(2)–B(2)–B(1) (triangle II). Levels are at 0·05 e Å^{-3}, negative contours are dotted. (*b*) Valence density distribution.

and 8 show the dynamic deformation densities and the corresponding valence densities in those triangles comprising four distinguishable B–B bonds (Table 2).

At first sight the various density patterns hardly reveal common bonding features and therefore interpretation is not without bias.

Two triangles (I) (Fig. 6*a*,*b*) lie on the top and bottom of the icosahedron. They are equilateral due to the threefold axis perpendicular to the plane. The deformation density shows a significant peak at the center (0·19 e Å^{-3}) and three peaks outside the triangle (0·17 e Å^{-3}). These charge accumulations can be considered as resulting from three-center interactions giving rise to bending of the bonds. Similar features are apparent in cyclopropane (Smith, 1977), decaborane (Brill, Dietrich & Dierks, 1971), or metallic beryllium (Yang & Coppens, 1978). *Ab initio* molecular-orbital calculations for the B_6 octahedron (Armstrong, Perkins & Stewart, 1971) also show a charge concentration at the centers of the triangular faces of the octahedron.

Table 2. B–B–B *triangles and* B–B *bonds in the* B_{12} *icosahedron*

	Triangles	B–B bonds		in
(I)	B(2)–B(2)–B(2)	B(2)–B(2)	1·821 Å	(I)
(II)	B(2)–B(2)–B(1)	B(2)–B(1)	1·807	(II), (III)
(III)	B(2)–B(1)–B(1)	B(2)–B(1)	1·796	(III)
		B(1)–B(1)	1·773	(III)

The triangle (II) (Fig. 7*a*,*b*) is perpendicular to a mirror plane. Again we find a central peak (0·27 e Å^{-3}) and extension of density beyond the B(1)–B(2) edges. The central peak is shifted towards B(2)–B(2) and connected with the external B(2)–B(2) peak in Fig. 6(*a*). This can be seen in Fig. 4, since this section is in the mirror plane cutting perpendicularly through the above two triangles. The results of this distribution are

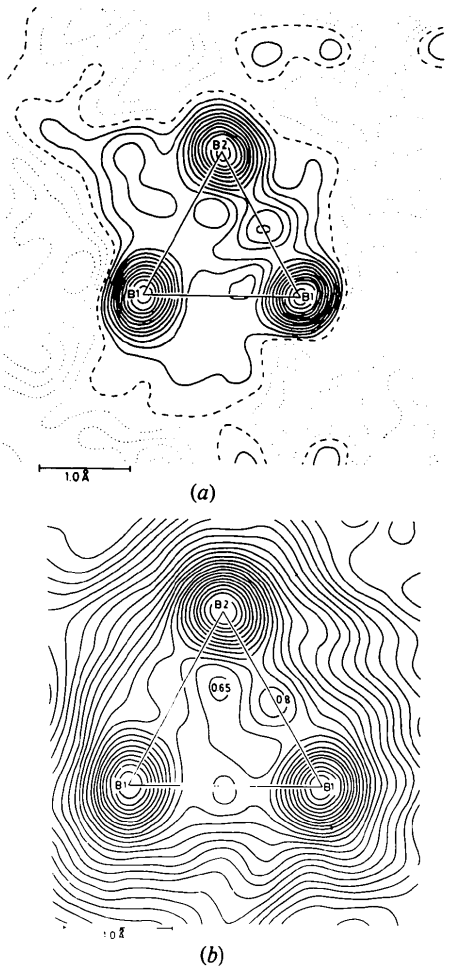

Fig. 8. (*a*) Dynamic deformation density distribution in the plane through B(2)–B(1)–B(1) (triangle III). Levels are at 0·05 e Å^{-3}, negative contours are dotted. (*b*) Valence density distribution.

density bumps on the surface of the icosahedron between the atoms.

The remaining triangle (III) B(1)–B(1)–B(2) (Fig. 8*a*,*b*) is completely asymmetric. Strong interaction (0·30 e Å^{-3}) is found between B(1) and B(2) lying on the mirror plane, but there is still a residue of the central peak observable in the section depicted in Fig. 9 which is perpendicular to the latter triangle.

Thus, all these findings may be interpreted in terms of three-center interactions for the triangles; however, the electron distribution is differently distorted from regularity due to different external forces.

The external bonds are B(2)–B(2) connecting adjacent icosahedra and B(1)–C providing the connection with the C–B–C chain. The deformation density distributions of both types of bonds can be seen in Fig. 4(*a*). A well developed bond overlap is found between the B(2) atoms (0·27 e Å^{-3}), indicating that the bonding between the icosahedra is of considerable strength. For the C–B(1) bond we do not find a bond peak, but there is still a saddle point with a significant density of 0·18 e Å^{-3} and the band of charge accumulation is rather broad. A better view may be obtained from Fig. 10, which shows the deformation density in the ring plane constituted by the B(1) atoms of two icosahedra and the connecting C atoms. This planar atomic arrangement forms a hexagon somewhat stretched in the C–C direction. Small but still significant bond peaks of almost 0·1 e Å^{-3} are found between the B(1) atoms, and hence the B(1) and C atoms can be regarded as forming infinite puckered layers of hexagons, in which each atom has three layer neighbors (comparable to graphite).

Confining oneself to the predominant deformation density accumulations one can develop a very simple model of bonding in B_{12}. In Fig. 11 the arrows indicate the positions and shifts of the main charge concentrations observable from the deformation and valence density maps. These largest overlaps again form a distorted icosahedron. If we associate two electrons with each overlap and add the 12 electrons associated with the external bonds, the 36 valence electrons of the B_{12} icosahedron are accommodated. Then we can deduce from Fig. 11 that, with respect to the pseudo fivefold axis, B(1) and B(2) possess different environments as depicted schematically in Fig. 11(*b*).

The environments indicate for B(1) a tendency towards *sp* hybridization and for B(2) a tendency towards sp^3 hybridization of the valence electrons. This view implies that the highly symmetric and delocalized valence-electron distribution of the ideal B_{12} icosahedron suffers a loss of symmetry by development of more localized intraicosahedral bonds due to the aniso-

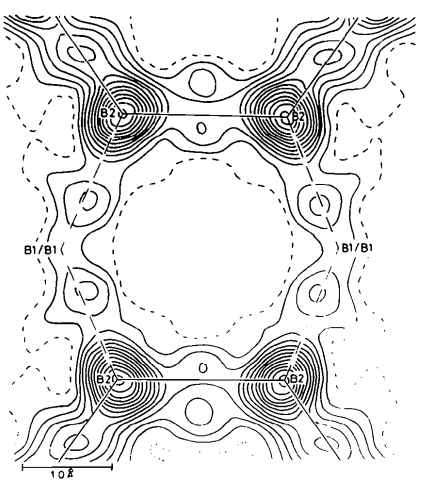

Fig. 9. Dynamic deformation density distribution in the plane through B(2), B(2) and the inversion center of the icosahedron. Levels are at 0·05 e Å^{-3}, negative contours are dotted.

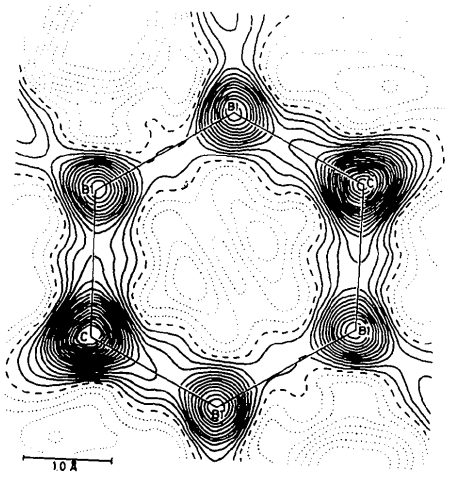

(a)

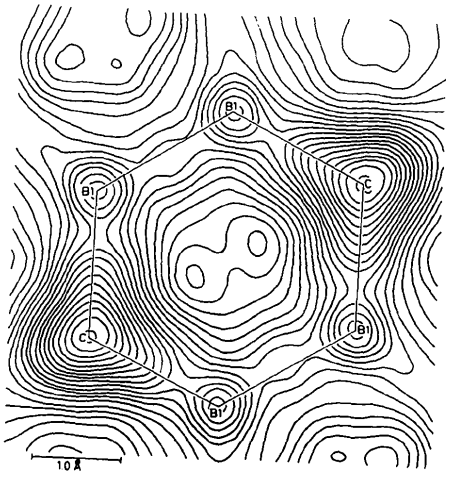

(b)

Fig. 10. (a) Dynamic deformation density distribution in the plane through the six-membered ring $B(1)_4C_2$. Levels are at 0·05 e Å^{-3}, negative contours are dotted. (b) Valence density distribution.

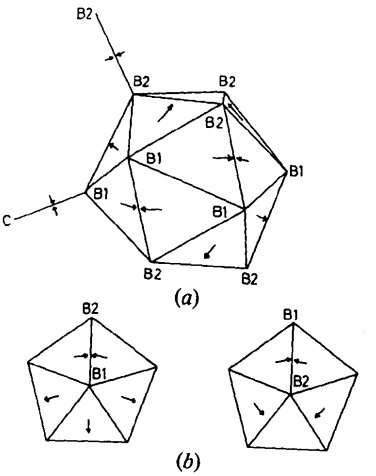

Fig. 11. (a) Schematic drawing of the B_{12} icosahedron and external bonds. Arrows indicate dominant deformation density accumulations. (b) Environments of B(1) and B(2) viewed along the pseudo fivefold axis (external bond direction).

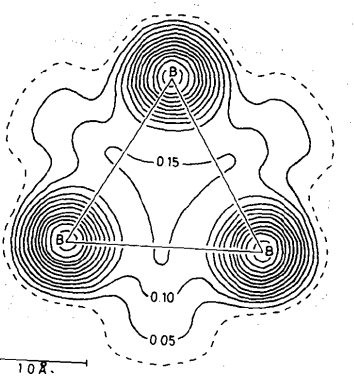

Fig. 12. Chemical average of the deformation density distribution in the icosahedral planes defined by triangular B–B–B arrangements. Levels are at 0·05 e Å^{-3}, negative contours are dotted.

tropic external bonding conditions and tends to become interpretable in terms of classic covalent bonding.

Of course, the true situation is somewhere between the above model and the ideal undisturbed B_{12} icosahedron and therefore one may as well approach the ideal charge distribution by treating the three unique triangular boron arrangements as equivalent. A chemical average was obtained by averaging the deformation density distributions in the planes through the triangles for all possible triangle orientations. The result is depicted in Fig. 12. A pile-up of the residual electron density of up to 0·18 e Å^{-3} is observed for the center of the triangular face. This density accumulation may be considered as providing Coulomb attraction of the positive nuclei and therefore as additional stabilizing elements of the highly symmetric arrangement of B atoms in the icosahedron. The charge extensions beyond the B–B connecting lines indicate bending of the direct B–B bonds similar to Fig. 6(a).

Conclusions

From the estimates of the accuracy of the difference density distribution we can assert for the present study that the charge accumulations on the bonds and on the icosahedral surface are significant. This is especially true for the C–B–C chain, for which the redistribution of electrons due to the bonding renders the conventional spherical-atom model inadequate. A reflection of this fact is given in the agreement indices of conventional all-data and HO refinements (part I).

Integrations of the observed density and valence density distribution associated with the C–B–C unit yielded charge estimates which give experimental evidence for a charge transfer towards the B_{12} icosahedron. However, it does not seem to be clear whether an electron is transferred in order to stabilize the B_{12} unit or to leave the chain to obtain a closed-shell configuration.

If the observed positions and heights of bond densities are taken into account it is possible to find an explanation for the extreme stability of the compound.

(i) The two structural units C–B–C and B_{12} possess strong internal bonds. For the B_{12} icosahedron the expected highly delocalized valence density distribution is disturbed by the icosahedral distortion and may be described to a first approximation in terms of normal covalent bonding. Then, the crystallographically different B(1) and B(2) atoms are chemically different as well in the sense that a tendency towards *sp* hybridization for B(1) and sp^3 hybridization for B(2) is observable. Since this must be a consequence of the chemically anisotropic environment of the B_{12} icosahedron, it should be of interest to study the geometric variation of the icosahedron and its electron distribution with different chemical environments [for example, C substituted by P (Spinar & Wang, 1962; Matkovich, 1961)].

(ii) Considering the development of more localized bonds; one finds the spatial distribution of all bonds including the external bonds to be approximately isotropic. Along the *c* axis bonding between the structural units is predominantly provided by B(2)–B(2) of adjacent icosahedra and within each icosahedron by B(2)–B(1). Bonding parallel to (001) is composed of the B(2)–B(2) contributions and the puckered hexagonal layers of B_4C_2 rings.

In the next stage of our study we plan to employ the results of the multipole expansion refinement (part I) in order to establish the corresponding static deformation density distributions, which may lead to an improved understanding of the chemical bonding in $B_{13}C_2$. *Ab initio* SCF calculations for the density distribution in the B_{12} icosahedron under consideration of the observed distortion from ideal symmetry have been started in cooperation with the Department of Theoretical Chemistry of the University of Bonn.

This work has received support from the Deutsche Forschungsgemeinschaft which is gratefully acknowledged.

References

ARMSTRONG, D. R., PERKINS, P. G. & STEWART, J. P. (1971). *J. Chem. Soc. A*, pp. 3674–3679.
BADER, R. F. W. (1975). *Acc. Chem. Res.* **8**, 34–40.
BRILL, R., DIETRICH, H. & DIERKS, H. (1971). *Acta Cryst.* B**27**, 2003–2018.
BUSING, W. R., MARTIN, K. O. & LEVY, H. A. (1962). *ORFLS*. Report ORNL-TM-305. Oak Ridge National Laboratory, Tennessee.
CRUICKSHANK, D. W. J. (1949). *Acta Cryst.* **2**, 65–82.
HAREL, M. & HIRSHFELD, F. L. (1975). *Acta Cryst.* B**31**, 162–172.
HIRSHFELD, F. L. (1971). *Acta Cryst.* B**27**, 769–781.
International Tables for X-ray Crystallography (1974). Vol. IV. Birmingham: Kynoch Press.
KIRFEL, A., GUPTA, A. & WILL, G. (1979). *Acta Cryst.* B**35**, 1052–1059.
KURKI-SUONIO, K. & SALMO, P. (1971). *Ann. Acad. Sci. Fenn. Ser. A*6, No. 369.
LONGUET-HIGGINS, H. C. & ROBERTS, M. DE V. (1955). *Proc. R. Soc. London Ser. A*, **230**, 110–119.
MATKOVICH, V. I. (1961). *Acta Cryst.* **14**, 93–94.
REES, B. (1976). *Acta Cryst.* A**32**, 483–488.
REES, B. (1978). *Acta Cryst.* A**34**, 254–256.
SMITH, V. H. (1977). *Phys. Scr.* **15**, 147–162.
SPINAR, L. H. & WANG, C. C. (1962). *Acta Cryst.* **15**, 1048–1049.
STEVENS, E. D. & COPPENS, P. (1975). *Acta Cryst.* A**31**, 612–619.
STEVENS, E. D. & COPPENS, P. (1976). *Acta Cryst.* A**32**, 915–917.
THOMAS, J. O. (1978). *Acta Cryst.* A**34**, 819–823.
WILSON, A. J. C. (1979). *Acta Cryst.* A**35**, 122–130.
YANG, Y. W. & COPPENS, P. (1978). *Acta Cryst.* A**34**, 61–65.